Energy Advances

ROYAL SOCIETY OF CHEMISTRY

PAPER

View Article Online
View Journal | View Issue

Cite this: *Energy Adv.*, 2025, 4, 94

Rational design of $NiMoO_4$/carbon nanocomposites for high-performance supercapacitors: an *in situ* carbon incorporation approach†

Raji Yuvaraja, [a] Sankar Sarathkumar, [a] Venkatesan Gowsalya, [a] Sorna Pandian Anitha Juliet, [a] Selvakumar Veeralakshmi, [b] Siva Kalaiselvam, [b] Gunniya Hariyanandam Gunasekar [cd] and Selvan Nehru *[a]

Understanding the impact of different compositions of nanocomposites synthesized *via in situ* incorporation of different ratios of carbon with metal oxides is an important factor for designing efficient electrode materials for high-performance supercapacitors. Here, a series of nanomaterials, $NiMoO_4$, carbonaceous nanospheres (CNSs), and $NiMoO_4$/C nanocomposites ($NiMoO_4$/C (Dx), where, x = 10, 25, 50, and 75 represents the molar ratio of dextrose (D) to Ni^{2+}), have been synthesized *via* an *in situ* hydrothermal method. The structural and surface analysis revealed the efficient integration of $NiMoO_4$ and carbon in the $NiMoO_4$/C (D50) nanocomposite, consisting of 71.1% $NiMoO_4$ and 28.9% carbon components. The nanocomposite features a graphitic carbon sheet-like structure embedded with $NiMoO_4$ nanorods, showing increased defects with higher carbon content and enhanced surface area with larger mesoporosity. In three-electrode supercapacitor studies for these electrode materials using 3 M KOH as the electrolyte, the $NiMoO_4$/C (D50)-based electrode delivered superior specific capacitance (940 F g^{-1}) at a current density of 1 A g^{-1} compared to bare $NiMoO_4$ (520 F g^{-1}), CNS (75 F g^{-1}) and $NiMoO_4$/C (D10, D25 and D75) nanocomposites (436–583 F g^{-1}), with 71% capacity retention up to 5000 cycles. Furthermore, for the fabricated $NiMoO_4$/C (D50)-based two-electrode supercapacitors at 1 A g^{-1} using 3 M KOH, the symmetric configuration delivered a doubled specific capacitance (83 F g^{-1}), while the asymmetric configuration led to a doubled performance in both energy density (14.2 W h kg^{-1}) and power density (444 W kg^{-1}), in comparison to each other. The enhanced supercapacitor performance of $NiMoO_4$/C (D50) can be attributed to the synergistic effect between carbon and $NiMoO_4$ in the optimized nanocomposites, which improves the electrolyte-philicity by altering the surface composition and properties, leading to more electroactive sites and increased charge storage capacity. Thus, designing new electrode materials *via in situ* hydrothermal synthesis of different metal oxide/C nanocomposites with optimal composition and choosing different carbon source materials will deliver high-performance supercapacitors in the near future.

Received 2nd July 2024,
Accepted 7th November 2024

DOI: 10.1039/d4ya00438h

rsc.li/energy-advances

1. Introduction

Supercapacitors (SCs) stand out among energy storage technologies due to their exceptional combination of rapid charge–discharge capabilities, outstanding cycling stability, inherent safety, and high power density.[1,2] Despite these advantages, their widespread applications are constrained by relatively lower energy density. To overcome this limitation, integrating hybrid nanocomposite materials consisting of pseudocapacitive metal oxides and capacitive carbon materials has emerged as a promising approach to achieve high energy density supercapacitors.[3,4] Among the different approaches, the *in situ* hydrothermal incorporation of carbon with metal oxides is particularly effective for tailoring electrode materials to surpassingly enhance their charge storage performance.[5,6] However, comprehensive reports on this specific approach for supercapacitors remain scarce in the existing literature.

Among various bimetallic oxides, nickel molybdate ($NiMoO_4$) emerges as a capable electrode material for SC owing

[a] *Department of Physical Chemistry, University of Madras, Guindy Campus, Chennai – 600025, Tamil Nadu, India. E-mail: nehruchem@gmail.com*
[b] *Centre for Industrial Safety, Anna University, Chennai – 600025, Tamil Nadu, India*
[c] *Department of Catalysis and Fine Chemicals, CSIR-Indian Institute of Chemical Technology, Hyderabad-500007, India*
[d] *CSIR-Academy of Scientific and Innovative Research (CSIR-AcSIR), Ghaziabad-201002, India*

† Electronic supplementary information (ESI) available. See DOI: https://doi.org/10.1039/d4ya00438h

to its key advantages, such as high specific capacitance accelerated by multiple redox states, enhanced electrical properties, reliable cyclability and moderate cost.[7] Notably, hydrothermal synthesis offers a versatile approach for producing $NiMoO_4$ with controlled and uniform morphology, high purity, scalability, and environmental friendliness. Moreover, this method enables the formation of diverse nanostructures of $NiMoO_4$ such as nanorods,[8] nanospheres,[9] nanosheets,[10] nanowires,[11] and nanoflowers,[12] each of which can significantly influence the SC performance of the resulting material.

However, during charge–discharge cycles, pristine $NiMoO_4$ undergoes volume expansion and structural degradation, leading to a decline in performance over time.[13] To address this limitation, researchers have explored composite electrodes that combine $NiMoO_4$ with carbonaceous nanomaterials. These materials offer several advantages, creating a synergistic effect that overcomes the inherent weaknesses of pristine $NiMoO_4$.[14] In particular, enhanced structural stability was offered by carbonaceous materials, including activated carbon, carbon fiber, graphene, carbon nanotubes, carbon aerogels, *etc.*, forming a conductive network around the $NiMoO_4$ particles. This network acts as a buffer, accommodating the volume changes experienced by $NiMoO_4$ during cycling and mitigating structural degradation. This significantly improves the cycling stability and lifespan of the supercapacitor.[15–18] Further, carbonaceous materials possess high surface areas, providing more sites for electrolyte interaction with the $NiMoO_4$, leading to higher capacitance. Additionally, their inherent conductivity enhances the overall electrical conductivity of the composite electrode, facilitating faster charge and discharge rates.[19] Several studies have demonstrated the effectiveness of this approach. For example, Muthu *et al.* reported that $NiMoO_4$/reduced graphene oxide composites exhibit increased surface area, enhancing capacitance.[20] Wei *et al.* synthesized carbon sphere@$NiMoO_4$ nanocomposites, resulting in improved overall electrical conductivity and faster charge–discharge rates.[21] Zhang *et al.* confirmed improved cycling stability and longer lifespan in $NiMoO_4$/carbon composites.[15] These findings highlight that the selection and optimization of $NiMoO_4$/carbon nanocomposites is essential for achieving high-performance supercapacitors.

Conversely, traditional methods for synthesizing carbon nanomaterials like carbon nanotubes and graphene often require complex procedures and high temperatures, significantly increasing their cost.[22,23] This high cost hinders their large-scale application in commercially viable supercapacitors. Hence, the potential of porous carbon derived from hydrothermal carbonization (HTC) as a cost-effective and sustainable alternative for supercapacitor electrodes has been explored. HTC utilizes readily available natural molecules such as sucrose, dextrose, and citric acid as carbon precursors.[24] This low-temperature process offers a simpler and more environmentally friendly approach to producing porous carbon materials. Mo *et al.* prepared a porous $NiCo_2O_4$@amorphous carbon nanocomposite using sucrose as a carbon source, resulting in a high specific capacity of 1225 mA h g^{-1}.[25] Similarly, an enhanced supercapacitor performance (specific capacity of 586 mA h g^{-1}) was reported by Zhang *et al.* in a NiO@carbon nanocomposite obtained from the blending of NiO with glucose-derived carbon.[26] However, the composition of carbon in the nanocomposites has to be optimized for the resulting enhancement effect in energy storage.

In particular, in comparison to the traditional blending approach, the incorporation of porous carbon with metal oxides through an *in situ* hydrothermal carbonization approach offers several advantages for supercapacitor applications. For example, Wang *et al.* reported *in situ* synthesis of noble metals with carbon reaching a specific capacitance of 115 F g^{-1} through the development of a porous carbon structure within the composite electrode.[27] Furthermore, Li *et al.* performed *in situ* synthesis of V_2O_3@C composites and achieved a specific capacitance of 205 F g^{-1} at 0.05 A g^{-1} *via* the improved intimate contact between the metal oxide and the carbon, creating a more efficient pathway for electron transfer throughout the electrode.[28] Ma *et al.* reported the *in situ* synthesis of a nitrogen-doped carbon framework with NiO nanoparticles, resulting in enhanced supercapacitor performance by providing more uniform particle size distribution, more active sites, smaller charge transfer resistance and higher ionic diffusion coefficient.[29] However, in these kinds of *in situ* synthesis of metal oxide/carbon nanocomposites, a comprehensive report on the influence of carbon content on the supercapacitor performance is not well elucidated in the literature.

Hence, the present work aims to investigate the impact of carbon content in $NiMoO_4$/carbon nanocomposites to be employed for supercapacitor applications. In particular, it focuses on (i) *in situ* hydrothermal synthesis of $NiMoO_4$/carbon nanocomposites with different amounts of carbon incorporation using dextrose as the carbon source, (ii) comparison of two- and three-electrode SC performance in terms of energy density, power density, specific capacitance and cycling stability, and (iii) fabrication and testing symmetric supercapacitor devices to evaluate their practical energy storage capability.

2. Experimental

2.1. Materials and methods

All chemicals were of analytical grade and used as such without any purification. Nickel nitrate hexahydrate, ammonium molybdate tetrahydrate, urea, hexamine, dextrose, sodium lauryl sulfate (SLS), potassium hydroxide and *N*-methyl pyrrolidine (NMP) were obtained from Sisco Research Laboratories Pvt. Ltd acetylene black (AB) and polyvinylidene fluoride (PVDF) were purchased from Sigma-Aldrich. Polyvinyl alcohol (PVA, M_w = ~115 000) was received from Loba Chemie Pvt. Ltd. Deionized (DI) water was used throughout the studies. Before use, the nickel plate (99% purity, thickness: 0.5 mm), and stainless-steel sheets (SS-304, thickness: 0.1 mm) were polished with P220 emery paper for surface activation, then sequentially cleaned in 1 M HCl for 15 minutes and acetone for 30 minutes using ultrasonication to remove any surface residues.

Synthesis of $NiMoO_4$. A modified hydrothermal synthesis of $NiMoO_4$ is as follows:[10] to a 25 mL aqueous solution of a

mixture of $Ni(NO_3)_2{\cdot}6H_2O$ (0.29 g, 1.0 mmol) and $(NH_4)_6Mo_7O_{24}{\cdot}4H_2O$ (1.24 g, 1.0 mmol), a 25 mL ethanolic solution of a mixture of urea (0.6 g, 10 mmol) and hexamine (1.4 g, 10 mmol) was added under constant stirring and allowed to stir for 30 min. The resultant solution was transferred into a Teflon-lined (100 mL) stainless steel autoclave, and heated in an oven at 180 °C for 12 h. The obtained greenish-yellow precipitate was filtered after cooling to room temperature, and washed three times with DI water and ethanol, followed by drying at 60 °C for 5 h. Then, the dried powder was calcinated in a muffle furnace at 400 °C for 3 h.

Synthesis of carbonaceous nanospheres (CNS). In a typical synthesis of carbonaceous nanospheres using the hydrothermal carbonization method.[30–32] A mixture of dextrose (0.36 g, 2.0 mmol) as a carbon source and SLS (0.58 g, 2.0 mmol) as a surfactant in 50 mL of water was vigorously stirred for 30 min. Then, the resultant solution was transferred into a Teflon-lined (100 mL) stainless steel autoclave, followed by heating at 180 °C for 12 h. The obtained black precipitate was filtered after cooling to room temperature, washed three times with DI water and ethanol, and dried in an oven at 60 °C for 5 h.

***In situ* hydrothermal synthesis of $NiMoO_4$/C (D*x*) nanocomposites.** To a 15 mL aqueous solution of a mixture of dextrose (1.8 g, 10 mmol) and SLS (2.88 g, 10 mmol), a 10 mL aqueous solution of a mixture of $Ni(NO_3)_2{\cdot}6H_2O$ (0.29 g, 1.0 mmol) and $(NH_4)_6Mo_7O_{24}{\cdot}4H_2O$ (1.24 g, 1.0 mmol) was added and ultrasonicated for 30 min. Then, a 25 mL ethanolic solution of a mixture of urea (0.6 g, 10 mmol) and hexamine (1.4 g, 10 mmol) was added to the reaction mixture under constant stirring and allowed to stir for 30 min. The obtained mixture was transferred into a Teflon-lined (100 mL) stainless steel autoclave, and heated in an oven at 180 °C for 12 h. The resultant black precipitate was filtered after cooling to room temperature, washed three times with water and ethanol, and dried in an oven at 60 °C for 5 h. Then, the dried powder was calcinated in a muffle furnace at 400 °C for 3 h.

The same procedure was followed to synthesise different compositions of $NiMoO_4$/C nanocomposites by varying the amount of dextrose as 25, 50 and 75 mmol. The prepared samples were labelled as $NiMoO_4$/C (D*x*), where x = 10, 25, 50 and 75, representing the molar ratio of dextrose/Ni^{2+}.

2.2. Materials characterization

X-Ray diffraction (XRD) patterns of the samples were obtained using a Bruker D8 Advance X-ray diffractometer with Cu-Kα radiation as the X-ray source in the 2θ range of 10°–90°. Raman spectra of the samples were collected from a Horiba Raman spectrometer using a 532 nm laser source. Fourier transform infrared (FT-IR) spectroscopy was performed on a Bruker mid-IR spectrometer. The thermogravimetric analysis (TGA) of the samples was carried out using a TGA Q500 V20.13 Build 39 thermal analyzer in an air atmosphere from 30 to 700 °C with a heating rate of 10 °C min^{-1}. Surface morphology and chemical elements of the samples were examined by a CARL ZEISS GEMINI 500 field emission scanning electron microscope (FE-SEM) coupled with energy dispersive X-ray spectroscopy (EDS). High-resolution transmission electron microscopy (HR-TEM) was performed on a FEI-TECNAI G2-20 TWIN microscope. BET surface area and BJH pore size distribution of the samples were obtained from the N_2 adsorption–desorption isotherm technique using a BELSORP II (BEL Japan Inc.) instrument. X-Ray photoelectron spectroscopy (XPS) was carried out on a PHI 5000 Versa Probe III photoelectron spectrometer (ULVAC-PHI, Inc., Japan) equipped with a monochromatic Al Kα source (λ = 1486.7 eV). All electrochemical measurements were carried out using the K-Lyte 1.3 (PG-Lyte) electrochemical workstation (Kanopy Techno Solutions, India). Electrochemical impedance spectroscopy (EIS) measurements were performed using the CHI660E workstation in the frequency range of 0.1 Hz to 100 kHz with a potential amplitude of 10 mV.

2.3. Electrochemical measurements

2.3.1 Three-electrode supercapacitor studies. To perform three-electrode SC studies, platinum wire, Hg/HgO electrode and aqueous 3 M KOH were used as the counter electrode, reference electrode and electrolyte, respectively. Furthermore, the working electrode was made from a slurry consisting of active material (80 wt%), acetylene black (10 wt%) as conducting material, and PVDF (10 wt%) as a binder using the requisite amount of NMP as the solvent. Then, the resultant slurry was coated on the surface of the nickel plate current collector (1.5 cm × 1.5 cm), followed by drying at 60 °C for 5 h. The mass loading of active materials on the nickel plate was calculated by weighing the plate before and after the loading of the active material. Cyclic voltammetry (CV) experiments were performed in the potential range of 0 to 0.6 V at various scan rates (10, 20, 40, 60, 80 and 100 mV s^{-1}). Galvanostatic charge–discharge (GCD) studies were assessed between the potential window of 0 to 0.5 V at different current densities (1, 2, 3, 4, 5, 10 and 15 A g^{-1}). The specific capacitance (C_s) values of the electrode materials were calculated from the GCD curves using eqn (1).[33]

$$C_s = \frac{I \times \Delta t}{m \times \Delta V} \quad (1)$$

where C_s (F g^{-1}), I (A), Δt (s), ΔV (V) and m (g) represent the specific capacitance, constant discharge current, time taken for discharging, potential drop upon discharging and mass loading of the active material on the electrode, respectively.

2.3.2 Two-electrode symmetric and asymmetric SC studies. For the two-electrode SC studies, symmetric SC was fabricated using a Swagelok-type cell by sandwiching the two symmetric electrodes using Whatman filter paper as the separator and 3 M KOH as the electrolyte. The symmetric electrodes were made by coating the slurry of active material consisting of $NiMoO_4$/C (D50) (80 wt%), PVDF (10 wt%), and acetylene black (10 wt%) using NMP solvent on two stainless steel (SS) plates (diameter: 1.7 cm and active area: 2.27 cm^2), followed by drying at 60 °C for 5 h. By following the same method, the asymmetric two-electrode SC was constructed except one of the electrodes consists of active material as acetylene black (90 wt%) and PVDF (10 wt%). From the obtained GCD curves, the performance of the two-electrode SCs was assessed by using eqn (2)–(4) for the

symmetric setup and eqn (5)–(7) for the asymmetric configuration.[33,34]

For the symmetric configuration,

$$C_s = 2 \times \frac{I \times \Delta t}{m \times \Delta V} \quad (2)$$

$$E = \frac{C_s \times (\Delta V)^2}{8 \times 3.6} \quad (3)$$

$$P = \frac{E}{\Delta t} \times 3600 \quad (4)$$

For the asymmetric configuration,

$$C_s = \frac{I \times \Delta t}{m' \times \Delta V} \quad (5)$$

$$E = \frac{C_s \times (\Delta V)^2}{2 \times 3.6} \quad (6)$$

$$P = \frac{E}{\Delta t} \times 3600 \quad (7)$$

where E is the energy density (W h kg^{-1}), P is the power density (W kg^{-1}), m stands for the mass loading of the active material in one electrode for symmetric type (g), and m' is the total mass loading of the active materials in both the anode and cathode for the asymmetric type (g).

2.3.3 Fabrication of all-solid-state symmetric SCs. All-solid-state SCs were fabricated using PVA-KOH gel electrolyte as follows:[35] firstly, PVA powder (3 g) in DI water (30 mL) was warmed to 80 °C and stirred continuously until the solution turned clear. Then, aqueous KOH (1.5 g, 20 mL) was vigorously added to the above solution at 80 °C until a clear solution was obtained. For the fabrication of symmetric SC devices, the electrodes were made by coating the slurry of active material consisting of $NiMoO_4$/C (D50) (80 wt%), PVDF (10 wt%), and acetylene black (10 wt%) using NMP on the six stainless steel (SS) plates (4.0 cm × 1.0 cm), followed by drying at 60 °C for 5 h. After that, the electrodes were dipped for 5 minutes in the hot PVA-KOH gel solution, followed by taking them out and allowing for solidification at room temperature. Furthermore, by hard pressing the two electrodes, a three-set of symmetric SC devices was made and tested for open-circuit potential (OCP) measurement. Then three sets of symmetric SC devices were coupled in series and activated through the cyclic voltammetry method for 10 cycles. After charging, the device was tested to lighten a blue LED to evaluate the SC performance for real-time applications.

3. Results and discussion

3.1. Synthesis and characterization of $NiMoO_4$/C nanocomposites

A typical *in situ* hydrothermal synthesis of $NiMoO_4$/C nanocomposite is illustrated in Scheme 1. There are two parallel reactions, namely, (i) the formation of $NiMoO_4$ by the combination of Ni^{2+} and MoO_4^{2-} ions by the urea and hexamine, which can act as both an alkali source and shape-controlling agent, and

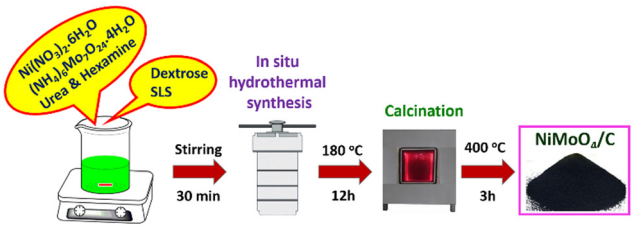

Scheme 1 Schematic representation of *in situ* hydrothermal synthesis of the $NiMoO_4$/C nanocomposite.

(ii) the formation of CNS material by the hydrothermal carbonization of dextrose using SLS as a templating agent.[24,31] By changing the molar ratio of dextrose, different amounts of carbon incorporated $NiMoO_4$/C nanocomposites were prepared to investigate the impact of their compositions on the supercapacitor performance. Furthermore, this kind of *in situ* incorporation of carbon with metal oxides as well as the influence of their composition on supercapacitor performance is not clear in the literature.

The X-ray diffraction method was used to study the structure and crystallinity of the electrode materials. Fig. 1(a)–(e) depicts typical XRD patterns of the synthesized CNS, $NiMoO_4$, and $NiMoO_4$/C (D*x*) samples. A broad peak corresponding to the (002) plane in Fig. 1(a) demonstrates the existence of a graphitic-like nature in CNS.[36] The XRD pattern in Fig. 1(b) matches the typical monoclinic structure of $NiMoO_4$ (JCPDS No. 86-0361), showing the characteristic peaks at 2θ values of 12.9°, 23.3°, 25.7°, 27.3°, 28.9° 33.1°, 33.8°, 39.1°, 46.5°, 49.4°, 55.4°, 56.5°, and 64.7° with respect to (001), (021), (−202), (−221), (220), (−312), (112), (−132), (240), (312), (223), (332), and (600) planes.[8,21] Furthermore, the formation of $NiMoO_4$/C (D*x*) nanocomposites can be confirmed from the observation of the characteristic diffraction pattern of $NiMoO_4$ in Fig. 1(c)–(e). However, in Fig. 1(c)–(e), the (002) diffraction peak of carbon merges with the $NiMoO_4$ peak at 24.8°, which may be due to the well-blended nature or suppression of carbon in the prepared nanocomposites.[16,21]

The Raman spectra of $NiMoO_4$, CNS and $NiMoO_4$/C-based nanocomposites are depicted in Fig. 2(a)–(e). The formation of

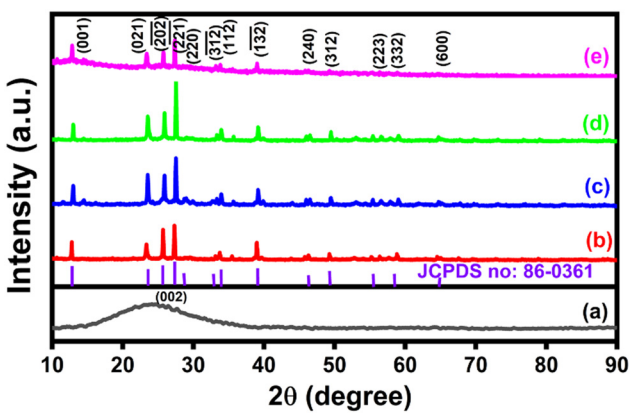

Fig. 1 XRD patterns of (a) CNS, (b) $NiMoO_4$, (c) $NiMoO_4$/C (D25), (d) $NiMoO_4$/C (D50) and (e) $NiMoO_4$/C (D75).

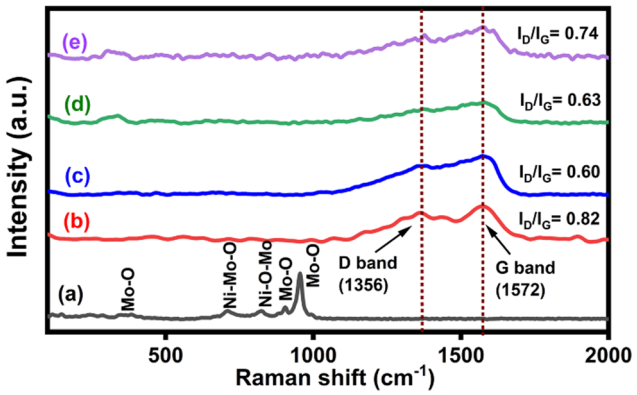

Fig. 2 Raman spectra of (a) $NiMoO_4$, (b) CNS, (c) $NiMoO_4$/C (D25), (d) $NiMoO_4$/C (D50) and (e) $NiMoO_4$/C (D75).

$NiMoO_4$ can be ascribed from the observation of bands at 384, 711, 825, 905, and 955 cm^{-1} (Fig. 2(a)) corresponding to the Mo–O bending, Ni–Mo–O symmetric stretching, Ni–O–Mo asymmetric stretching, Mo–O asymmetric stretching and Mo–O symmetric stretching modes, respectively.[37,38] The Raman spectrum of CNS in Fig. 2(b) shows the characteristic D and G bands of carbon at 1356 cm^{-1} and 1572 cm^{-1} corresponding to the defects caused by the out-of-plane and in-plane vibrations in the graphitic structure, respectively.[16] Furthermore, the characteristic peaks associated with $NiMoO_4$ in the prepared nanocomposites Fig. 2(c)–(e) are masked due to the presence of higher carbon content. The obtained values of I_D/I_G ratio for CNS, $NiMoO_4$/C (D25), $NiMoO_4$/C (D50) and $NiMoO_4$/C (D75) are 0.82, 0.60, 0.63, and 0.74, respectively. The noted increase in the I_D/I_G ratio of the $NiMoO_4$/C nanocomposites with the increase in carbon content suggests an increase in the defects of the graphitic structure.[39]

The FT-IR spectra of CNS, $NiMoO_4$ and $NiMoO_4$/C (D25, D50 and D75) in Fig. 3(a)–(e) were used to analyze their characteristic vibrational modes and chemical bonding environment. In Fig. 3(a), the FTIR spectrum of CNS exhibits characteristic peaks at 3675–3000 cm^{-1} (O–H stretching), 2925 cm^{-1} & 2850 cm^{-1} (C–H stretching), 1700 cm^{-1} (C═O stretching), 1612 cm^{-1} (C═C stretching), 1470–1350 cm^{-1} (combination of O–C–H and C–O–H absorption bands), 1198 cm^{-1} (in-plane C–H and O–H deformation), 1190–970 cm^{-1} (C–O and C–C stretching) and 880–750 cm^{-1} (aromatic C–H out-of-plane bending), supporting the presence of carboxylic acid, carbonyl, olefin, and hydroxyl groups within the graphitic carbon structure of CNS.[40–42] The spectrum of $NiMoO_4$ in Fig. 3(b) displays an intense peak at 928 cm^{-1}, corresponding to the symmetric stretching vibrations of Mo═O bonds of the distorted MoO_4 lattice. Additionally, sharp peaks at 397 and 582 cm^{-1} are attributed to Mo–O–Mo and Mo–O–Ni vibrations, respectively.[43–45] Furthermore, the prepared $NiMoO_4$/C (D25, D50 and D75) nanocomposites in Fig. 3(c)–(e) exhibit characteristic vibrations, with slight variations in intensity and position corresponding to the increase in carbon content, suggesting a noticeable interaction between $NiMoO_4$ and carbon within the nanocomposite structure.[46,47]

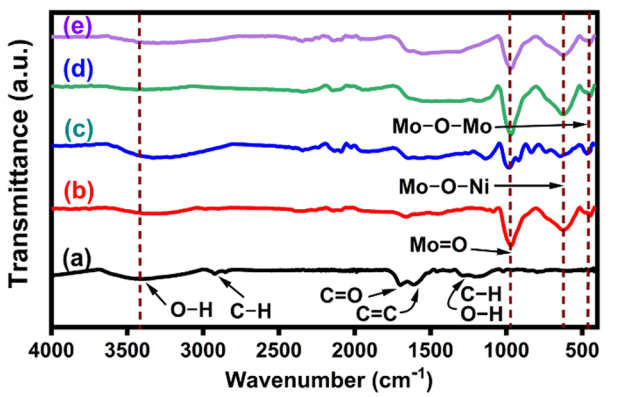

Fig. 3 FT-IR spectra of (a) CNS, (b) $NiMoO_4$, (c) $NiMoO_4$/C (D25), (d) $NiMoO_4$/C (D50) and (e) $NiMoO_4$/C (D75).

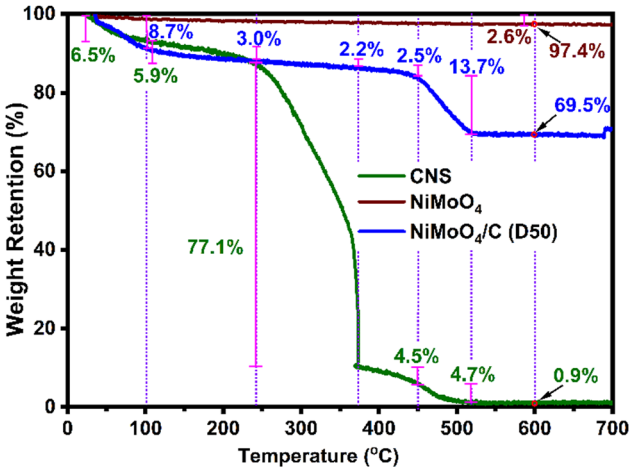

Fig. 4 TGA profiles of CNS, $NiMoO_4$, and $NiMoO_4$/C (D50).

To further elucidate the composition of $NiMoO_4$ in the as-prepared nanocomposite, TGA was conducted for CNS, $NiMoO_4$ and $NiMoO_4$/C (D50), as shown in Fig. 4. $NiMoO_4$ exhibits excellent thermal stability, retaining 97.4% of its initial weight at 600 °C with a minimal weight loss of 2.6%. In contrast, CNS shows significant weight losses of 6.5%, 5.9%, 77.1%, 4.5%, 4.7%, and 0.4% in the temperature ranges of 30–100 °C, 100–240 °C, 240–370 °C, 370–450 °C, 450–520 °C, and 520–600 °C, respectively. Similarly, $NiMoO_4$/C (D50) displays weight losses of 8.7%, 3.0%, 2.2%, 2.5%, 13.7%, and 0.4% across the same temperature ranges. These observed weight losses are likely due to (i) the removal of moisture and volatile substances between 30–240 °C, (ii) the decomposition of organic groups between 240–370 °C, and (iii) the decomposition of residual organics between 370–520 °C.[48–50] Notably, at 600 °C, nearly all carbon content in the $NiMoO_4$/C (D50) nanocomposite is lost (CNS weight reduced to 0.9%), while $NiMoO_4$ remains largely intact, retaining 97.4% of its weight. Therefore, the calculated $NiMoO_4$ and carbon components in the $NiMoO_4$/C (D50) nanocomposite were determined to be 71.1% and 28.9%, respectively (refer to ESI† for calculation).

The FESEM images of pure $NiMoO_4$, CNS and $NiMoO_4$/C (D50) in Fig. 5(a)–(c) are used to correlate the impact of their

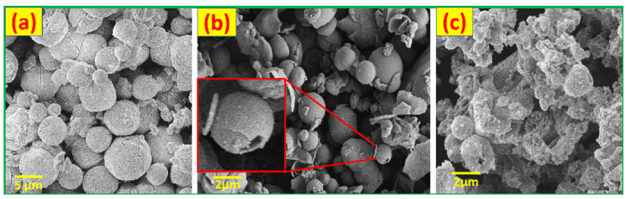

Fig. 5 FESEM images of (a) $NiMoO_4$, (b) CNS and (c) $NiMoO_4$/C (D50).

structural features on the supercapacitor performance. In Fig. 5(a), $NiMoO_4$ appears as hierarchical porous microspheres with an average diameter of 3.0 μm.[9,51,52] The as-prepared CNS in Fig. 5(b) looks like hollow nano/microspheres (740 nm–1.7 μm).[31] However, the preparation of the $NiMoO_4$/C (D50) nanocomposite results in aggregated/collapsed microspheres in Fig. 5(c) due to the blending $NiMoO_4$ and carbon in the nanocomposite. The presence of Ni, Mo, O and C elements in the prepared $NiMoO_4$, CNS and $NiMoO_4$/C (D50) was further confirmed by EDAX analysis (Fig. S1, ESI†). Thus, the effective blended and porous nature of the prepared nanocomposite may afford more electrochemical active sites for more charge storage.[21]

The morphology of the $NiMoO_4$/C (D50) nanocomposite was further examined using HRTEM, as shown in Fig. 6(a)–(d). The HRTEM images in Fig. 6(a) and (b) reveal a graphitic carbon sheet-like structure with embedded $NiMoO_4$ nanorods, indicating the efficient integration of $NiMoO_4$ within the carbon matrix of the nanocomposite. This highlights the effectiveness of the *in situ* carbon incorporation approach in achieving a homogeneously dispersed nanostructure, superior to conventional blending methods.[53] Fig. 6(c) displays lattice fringes with a spacing of 0.31 nm, corresponding to the (220) plane of monoclinic $NiMoO_4$. The selected area electron diffraction (SAED) pattern in Fig. 6(d) further confirms the polycrystalline nature of $NiMoO_4$ within the $NiMoO_4$/C (D50) nanocomposite.[54]

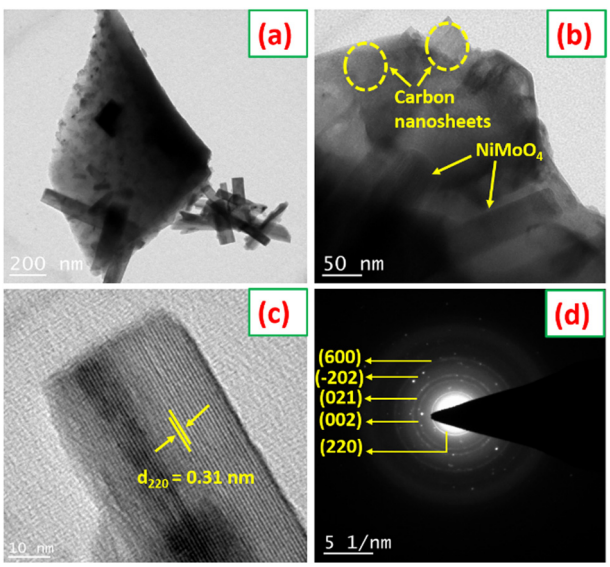

Fig. 6 (a)–(d) HRTEM images of $NiMoO_4$/C (D50) with the SAED pattern.

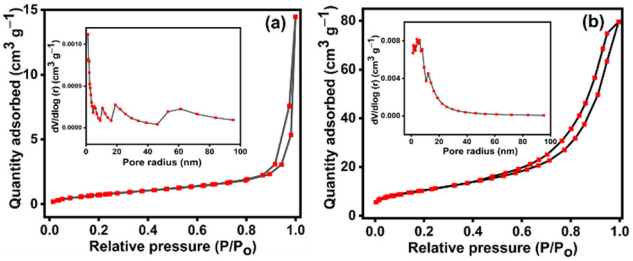

Fig. 7 N_2 adsorption–desorption BET isotherms with corresponding BJH pore-size distributions plots (insets): (a) $NiMoO_4$ and (b) $NiMoO_4$/C (D50).

BET isotherms of N_2 adsorption–desorption along with BJH pore size distribution plots for $NiMoO_4$ and $NiMoO_4$/C (D50) are shown in Fig. 7(a) and (b) to elucidate their surface area and pore size distribution. Both samples exhibit type IV isotherms with H3 hysteresis loops, indicative of mesoporous materials. Both $NiMoO_4$ and $NiMoO_4$/C (D50) initially show a gradual increase in N_2 adsorption with increasing relative pressure due to the presence of mesopores involving capillary reduction and multilayer adsorption. Lastly, a rapid rise in the adsorption at the high-pressure region explores the occurrence of adsorption within the interstices between the nanoparticles. Furthermore, the pore size distribution plots in Fig. 7((a) and (b) insets) also reveal the coexistence of mesopores (2–50 nm) and macropores (>50 nm) in the prepared $NiMoO_4$ and $NiMoO_4$/C (D50) nanocomposite. Besides the incorporation of carbon significantly 12-fold increases the BET surface area of the $NiMoO_4$/C (D50) nanocomposite (37.4 $m^2\ g^{-1}$) compared to pure $NiMoO_4$ (2.93 $m^2\ g^{-1}$). However, the pore volume and pore radius of the nanocomposite (0.015 $cm^3\ g^{-1}$ and 13.9 nm, respectively) are lower compared to $NiMoO_4$ (0.12 $cm^3\ g^{-1}$ and 20.8 nm), likely due to the effective blending of $NiMoO_4$ and carbon in the nanocomposite.[10,39,55] The observed higher surface area and larger mesoporosity of the $NiMoO_4$/C (D50) nanocomposite may offer more electroactive sites and efficient pathways for electron transport to facilitate faster redox processes and more charge storage.[8,51,56]

The chemical structure and bonding characteristics of $NiMoO_4$/C (D50) were further confirmed by elucidating their XPS spectra of Mo 3d, Ni 2p, O 1s, and C 1s elements (Fig. 8(a)–(d)). The Ni 2p spectrum in Fig. 8(a) shows two distinct spin–orbit doublets corresponding to Ni $2p_{3/2}$ (856.2 eV) and Ni $2p_{1/2}$ (873.9 eV), along with shakeup satellite peaks at 861.8 and 880.1 eV for each doublet, respectively. Furthermore, the deconvolution of each doublet presents two peaks corresponding to the coexistence of Ni^{2+} (855.9 and 873.4 eV) and Ni^{3+} (856.9 and 875.2 eV). The Mo 3d spectrum (Fig. 8(b)) exhibits two distinct peaks at 232.5 and 235.6 eV corresponding to Mo $3d_{5/2}$ and Mo $3d_{3/2}$ levels of Mo^{6+}, correspondingly. These findings explore the coexistence of Ni^{2+}/Ni^{3+} and Mo^{6+} species in the $NiMoO_4$/C (D50) nanocomposite.[1,8,51] Furthermore, the deconvoluted O 1s spectrum (Fig. 8(c)) dictates two peaks at 530.5 and 532.0 eV, respective to the existence of primary lattice oxygen species associated with metal–oxygen bonds and defect sites of lattice oxygen by the insufficient coordination in

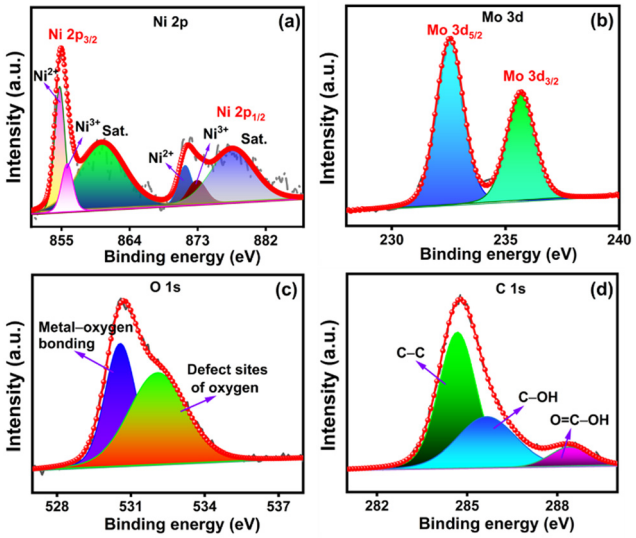

Fig. 8 XPS spectra of $NiMoO_4$/C (D50): (a) Ni 2p, (b) Mo 3d, (c) O 1s and (d) C 1s.

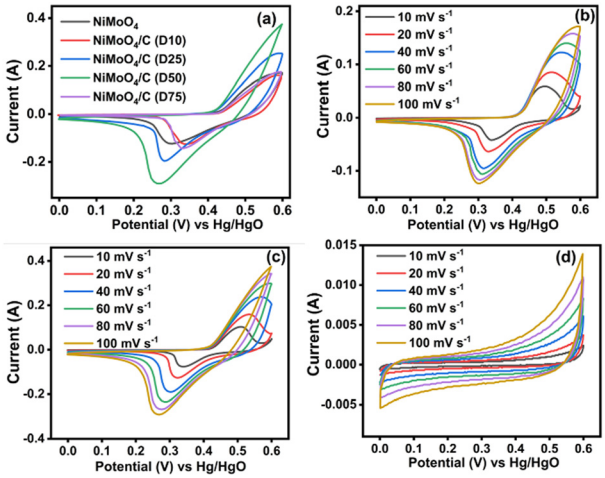

Fig. 9 CV curves at different scan rates: (a) comparison data of $NiMoO_4$ and $NiMoO_4$/C (D*x*) at 100 mV s^{-1}, (b) $NiMoO_4$, (c) $NiMoO_4$/C (D50) and (d) CNS.

$NiMoO_4$ or oxygenated species of carbon. The deconvoluted C 1s spectrum of carbon in Fig. 8(d) reveals a prominent peak for C–C at 284.6 eV and other weaker peaks for C–OH (285.6 eV) and O═C–OH (288.3 eV).[57,58]

3.2. Three-electrode supercapacitor studies

Three electrode SC studies for $NiMoO_4$, CNS, and $NiMoO_4$/C (D*x*)-based electrode materials coated on a nickel plate were examined in 3 M KOH electrolyte at different sweep rates (10 to 100 mV s^{-1}) in the potential range of 0 to 0.6 V (*vs.* Hg/HgO). Fig. 9(a) shows a set of redox peaks at about 0.43–0.51 V and 0.31–0.39 V in the CV profiles of $NiMoO_4$ and $NiMoO_4$/C (D*x*) at a sweep rate of 100 mV s^{-1}, dictating the involvement of pseudocapacitive behavior by the Ni^{2+}/Ni^{3+} redox couple through the faradaic reactions corresponding to Ni–O/Ni–O–OH redox transitions (eqn (8) and (9)) on the electrode surfaces in the alkaline medium.[44,55]

$$NiMoO_4 + 2OH^- \leftrightarrow Ni(OH)_2 + MoO_4^{2-} \quad (8)$$

$$Ni^{2+}(OH)_2 + OH^- \leftrightarrow Ni^{3+}OOH + H_2O + e^- \quad (9)$$

However, Mo species does not take part in redox reactions and it only helps to increase molybdate's conductivity, thereby resulting in enhanced supercapacitor performance.[15,59] Furthermore, all the electrode materials show a symmetrical CV profile, demonstrating the reversibility of these redox processes to be employed as efficient rechargeable supercapacitors. In particular, $NiMoO_4$/C (D50) shows a larger CV curve area and enhanced current response compared to $NiMoO_4$ and $NiMoO_4$/C (D10, D25, and D75), signifying that the optimum carbon incorporated nanocomposite can result in enhanced electrical conductivity and electrolyte-philicity *via* altering the surface composition and properties of the electrodes, with lowering charge transfer resistance to store more amount of charge.[60]

The impact of various scan rates (10–100 mV s^{-1}) on the CV profiles of all prepared electrodes are shown in Fig. 9(b)–(d) and Fig. S2a–c (ESI†). When increasing the scan rates for the $NiMoO_4$-based electrodes, both the anodic and cathodic peaks shift towards more positive and more negative potentials, respectively, signifying the involvement of faster electron and ion transfer reactions through pseudocapacitive faradaic mechanisms at the electrode–electrolyte boundaries.[8,10] Meanwhile, CNS (Fig. 9(d)) exhibits the characteristic rectangular/quasi-rectangular CV profiles associated with the electrical double layer capacitance (EDLC) of a non-faradaic process.[61–63]

The charge storage capability of the as-prepared electrodes was further evaluated using the GCD technique. Fig. 10(a) shows the comparative GCD curves of $NiMoO_4$ and $NiMoO_4$/C (D*x*)-based nanocomposites. The noted longest discharge time for the $NiMoO_4$/C (D50) electrode may result in more charge storage for attaining higher specific capacitance. Furthermore, the observed two voltage plateaus in the GCD curves of the $NiMoO_4$ and $NiMoO_4$/C (D*x*)-based nanocomposites depict the involvement of faradaic reactions as corroborated with CV results. All electrode materials show a low IR drop, representing their good conductivity and small internal resistivity for fabricating high-rate supercapacitors.[21,44] Furthermore, the noted asymmetrical shape of the GCD curves implies increased polarization. Also, the presence of loops in the GCD curves implies the involvement of faradaic reactions through the insertion/extraction of ions into and out of the $NiMoO_4$ lattice during charge/discharge cycles.[64]

The influence of different current densities (1–15 A g^{-1}) on the GCD curves of $NiMoO_4$, CNS, and $NiMoO_4$/C (D*x*) nanocomposites are shown in Fig. 10(b)–(d) and Fig. S3a–c (ESI†). At higher current densities, $NiMoO_4$-based electrode materials exhibit linear charge/discharge curves due to faster ion diffusion, which limits the rate of the faradaic charge storage mechanism. Conversely, at lower current densities, non-linear charge/discharge curves are observed due to increased contributions from faradaic reactions, resulting in more efficient charge storage.[65,66] To further quantitatively estimate the supercapacitor performance of the prepared electrode materials, specific capacitance

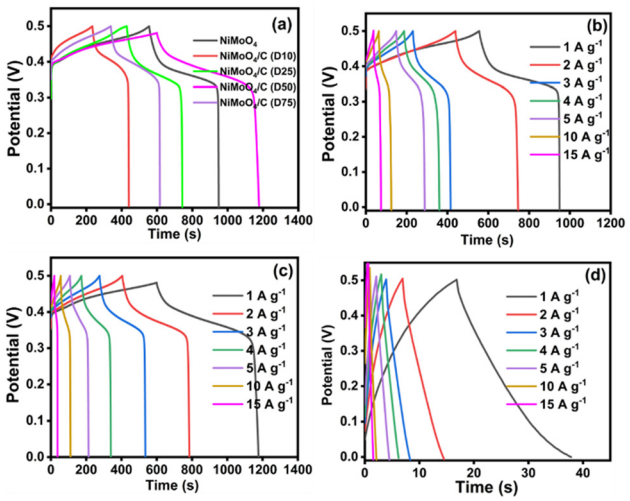

Fig. 10 GCD curves at different current densities: (a) comparison data of $NiMoO_4$ and $NiMoO_4$/C (D*x*) at 1 A g^{-1}, (b) $NiMoO_4$, (c) $NiMoO_4$/C (D50) and (d) CNS.

(C_s) was calculated from the GCD discharge curves using eqn (1) and the values are presented in Table S1 (ESI†). Notably, $NiMoO_4$/C (D50) demonstrates the highest specific capacitance (940 F g^{-1}) compared to pure $NiMoO_4$ (520 F g^{-1}), CNS (75 F g^{-1}), and other $NiMoO_4$/C (D*x*) nanocomposites (436, 583, and 508 F g^{-1} for D10, D25, and D75, respectively). Interestingly, the $NiMoO_4$/C (D50) nanocomposite exhibits a near-doubling of its specific capacitance compared to pure $NiMoO_4$. In contrast, other nanocomposites do not show a significant enhancement effect. This emphasizes that the incorporation of different amounts of carbon with $NiMoO_4$ could result in altering the surface composition and properties of the as-prepared electrodes. In particular, the dextrose-derived carbon is expected to consist of some polar moieties such as carboxylic acids, alcohols, carbonyl groups, *etc.*, which leads to deriving hydrophilic and hydrophobic regions on the electrode surface.[41] The presence of these regions is expected to alter the wettability or electrolyte-philicity of electrode materials. Thus, the existence of a synergistic effect between $NiMoO_4$ and the optimized carbon content in the $NiMoO_4$/C (D50) nanocomposite *via* improved electrolyte-philicity at the electrode surface results in enhanced electrochemical performance for more charge storage.[44,67]

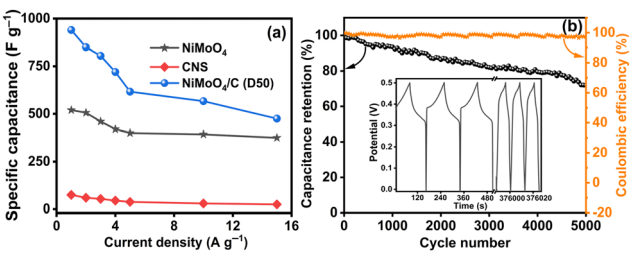

Fig. 11 (a) Comparison curves of the specific capacitances of the $NiMoO_4$, CNS and $NiMoO_4$/C (D50) at different current densities, and (b) capacity retention and coulombic efficiency of $NiMoO_4$/C (D50) up to 5000 cycles at 5 A g^{-1}. The inset figure shows the initial and final three cycles of the GCD curves.

Fig. 11(a) compares the specific capacitances of $NiMoO_4$, CNS, and $NiMoO_4$/C (D50) at various current densities (1 to 15 A g^{-1}), demonstrating the reliable performance of $NiMoO_4$/C (D50) across all tested current densities. As the current density decreases, $NiMoO_4$/C (D50) exhibits higher specific capacitance due to enhanced faradaic processes and increased electrolyte ion diffusion. Furthermore, the $NiMoO_4$/C (D50) electrode exhibits moderate charge–discharge rate capability, retaining approximately 51% of its specific capacitance when the current density is increased from 1 A g^{-1} to 15 A g^{-1}.[14,16] The long-term cycling stability and coulombic efficiency of the $NiMoO_4$/C (D50)-based electrode were evaluated by repeated GCD measurements up to 5000 cycles at 5 A g^{-1}, as shown in Fig. 11(b). The remarkable retention of 71% of its initial specific capacitance up to 5000 cycles demonstrates the appreciable cycling stability and resilience against degradation mechanisms of the $NiMoO_4$/C (D50) electrode. Furthermore, the noted coulombic efficiency remains nearly 96% even up to 5000 cycles, highlighting the efficient charge transfer and reversibility of the faradaic reactions.[16,66] Additionally, the FESEM images (Fig. 12(a) and (b)), taken before and after 5000 GCD cycles at 5 A g^{-1} for the $NiMoO_4$/C (D50) electrodes, illustrate the structural changes impacting supercapacitor performance after cyclic stability testing. The images reveal that the initially smooth electrode surfaces exhibit signs of fracturing or degradation following prolonged cycling, which consequently leads to a decline in supercapacitor performance.

EIS analysis of $NiMoO_4$, CNS and $NiMoO_4$/C (D50) provides valuable insights into the electrochemical behavior and interface properties of the electrode materials. The Nyquist plots (Fig. 13) were fitted with an equivalent circuit (inset Fig. 13) using ZSimpWin software to extract key electrical parameters (Table S2, ESI†). All the electrode materials show acceptable χ^2 values, indicating excellent fitting of the equivalent circuit. Solution resistance (R_s) for $NiMoO_4$/C (D50) (1.16 Ω cm^2) is comparable to $NiMoO_4$ (1.15 Ω cm^2) and CNS (1.07 Ω cm^2), indicating the minimal impact of carbon on bulk electrolyte resistance. Charge transfer resistance (R_{ct}), crucial for interfacial electron transfer, is significantly lower for $NiMoO_4$/C (D50) (2.96 Ω cm^2) compared to $NiMoO_4$ (13.02 Ω cm^2), but higher than CNS (55.8 μΩ cm^2), suggesting improved interfacial properties likely due to enhanced conductivity from the incorporated carbon. Pore resistance (R_{pore}) reflects ion diffusion

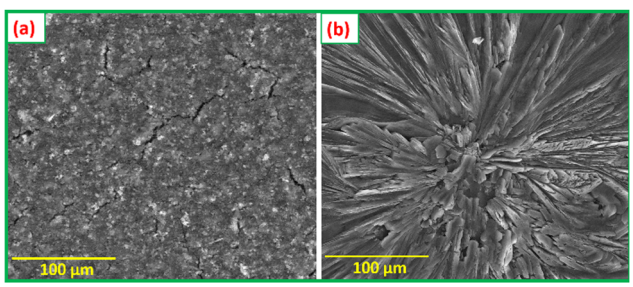

Fig. 12 FESEM images of the $NiMoO_4$/C (D50) electrode (a) before and (b) after cyclic stability studies performed for GCD 5000 cycles at 5 A g^{-1}.

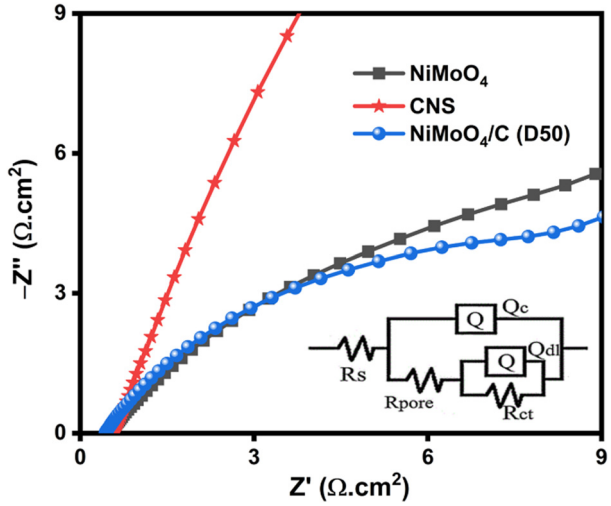

Fig. 13 EIS Nyquist plot of $NiMoO_4$, CNS and $NiMoO_4$/C (D50) samples with the inset of their equivalent circuit.

within the electrode. $NiMoO_4$/C (D50) displayed a slightly higher R_{pore} value (5.48 mΩ cm^2) compared to $NiMoO_4$ (0.95 mΩ cm^2) but much lower than CNS (57.7 mΩ cm^2). This indicates a more accessible pore network in the $NiMoO_4$/C (D50) composite, achieved by altering the surface composition and structure, leading to improved electrolyte penetration and ion diffusion compared to pure CNS.[68,69]

Constant phase elements (CPEs) provide insights into capacitance. We analyzed Q_c (coating capacitance) and Q_{dl} (double layer capacitance). Q_c values for $NiMoO_4$ (0.0032 S cm^{-2} s^n), CNS (0.0012 S cm^{-2} s^n), and $NiMoO_4$/C (D50) (0.0024 S cm^{-2} s^n) represent the porous structure's capacitance. The slightly lower Q_c for $NiMoO_4$/C (D50) suggests a potentially less developed pore network compared to pristine $NiMoO_4$. Q_{dl} values for $NiMoO_4$ (0.0229 S cm^{-2} s^n), CNS (0.0005 S cm^{-2} s^n), and $NiMoO_4$/C (D50) (0.0236 S cm^{-2} s^n) reflect the electrode–electrolyte interface capacitance. Comparable values for $NiMoO_4$ and $NiMoO_4$/C (D50) indicate minimal change in accessible surface area for ion adsorption with carbon incorporation. The lower Q_{dl} for CNS suggests limited capacitance due to its lower conductivity. The Warburg impedance (W) characterizes ion diffusion within the electrode. W values for $NiMoO_4$ (4.091×10^{-12} S cm^{-2} $s^{0.5}$), CNS (1.034×10^{-4} S cm^{-2} $s^{0.5}$), and $NiMoO_4$/C (D50) (6.465×10^{-12} S cm^{-2} $s^{0.5}$) reveal slower diffusion in CNS compared to $NiMoO_4$ and $NiMoO_4$/C (D50). This suggests that carbon facilitates ion transport in the composite while maintaining a comparable rate to pristine $NiMoO_4$. EIS analysis supports the benefits of the $NiMoO_4$/C (D50) composite structure. While the Q_c value suggests a potentially less developed pore network, the comparable Q_{dl} value indicates maintained accessible surface area. This highlights a potential trade-off between pore development and conductivity within the composite. The significantly lower R_{ct} and faster ion diffusion (W) in $NiMoO_4$/C (D50) compared to CNS demonstrate the positive impact of carbon, likely contributing to its enhanced electrochemical performance.[70–72]

To investigate the contribution of capacitive or diffusive controlled processes in the energy storage mechanism of $NiMoO_4$/C (D50), CV experiments were performed at various scan rates (1–10 mV s^{-1}) using three electrode configurations. The association between the current (i) *vs.* scan rate (ν) can be expressed by the following eqn (10) and (11):[44,73]

$$i = a \times \nu^b \quad (10)$$

$$\log(i) = \log(a) + b\log(\nu) \quad (11)$$

where a is constant, and b is the slope of the $\log(i)$ *vs.* $\log(\nu)$ graph.

Further, it is known that the value of b is 0.5 and 1 for the diffusion-controlled and capacitive-controlled processes, respectively.[73,74] The b values of the $NiMoO_4$/C (D50) electrode obtained from Fig. 14(a) indicate mixed behavior. For the anodic process, the intermediate b value (0.608) falls within the range of $0.5 < b < 1.0$, suggesting contributions from both diffusion and capacitive processes, *i.e.* the system is influenced by both the diffusion of ions and surface reactions. Conversely, the lower b value (0.052) for the cathodic process ($b < 0.5$) suggests a predominantly diffusion-controlled process with additional kinetic limitations, which may be due to factors such as slow electron transfer or mass transport resistances.[4,75]

To further estimate the contribution of the surface-controlled capacitive process ($k_1\nu$) and diffusion-controlled/faradaic process ($k_1\sqrt{\nu}$) methods on the current of the $NiMoO_4$/C (D50) electrode, the following eqn (12)–(15) were used:[73]

$$i = k_1\nu + k_2\sqrt{\nu} \quad (12)$$

or

$$i/\sqrt{\nu} = k_1\sqrt{\nu} + k_2 \quad (13)$$

$$\text{Capacitive contribution rate (\%)} = \frac{k_1\nu}{k_1\nu + k_2\sqrt{\nu}} \times 100\% \quad (14)$$

$$\text{Diffusive contribution rate (\%)} = \frac{k_2\sqrt{\nu}}{k_1\nu + k_2\sqrt{\nu}} \times 100\% \quad (15)$$

where the values of k_1 and k_2 were obtained from the plot of $i/\sqrt{\nu}$ *versus* $\sqrt{\nu}$ (Fig. 14(b)). The estimated contributions of capacitive-controlled (43%) and diffusion-controlled (57%) processes in the cyclic voltammogram of $NiMoO_4$/C (D50) at 10 mV s^{-1} are presented in Fig. 14(c). As shown in Fig. 14(d), increasing the scan rate from 1 mV s^{-1} to 10 mV s^{-1} leads to a progressive increase in the capacitive contribution from 19% to 43%, indicating a limitation in the diffusion time of electrolyte ions to reach the electrode surfaces at higher scan rate.[73,76]

3.3. Two-electrode symmetric and asymmetric SC studies

The electrochemical outcomes of $NiMoO_4$/C (D50) based symmetric and asymmetric SCs were evaluated at different scan rates (10–100 mV s^{-1}) using a Swagelok-type two-electrode setup and 3 M KOH electrolyte. The CV curves of both symmetric and asymmetric SCs exhibit no distinct redox peaks in Fig. 15(a) and (b). Unlike the symmetric SC, the asymmetric SC demonstrates a uniformly increased current response even upon increasing the

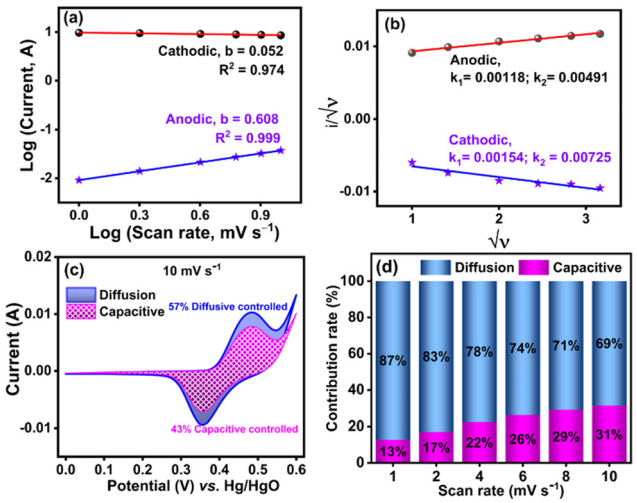

Fig. 14 Kinetics of energy storage behavior of $NiMoO_4$/C (D50) at different scan rates (1–10 mV s^{-1}): (a) plot of log(*i*) *vs.* log(*v*), (b) plot of $i/\sqrt{\nu}$ and $\sqrt{\nu}$, (c) CV cycles of capacitive-contribution (pink-shaded region) and diffusion-contribution (blue-shaded region) at 10 mV s^{-1}, and (d) total contribution rate of capacitive (pink) and diffusion-controlled (blue) processes at different scan rates.

scan rate, indicating its good rechargeable behavior for making it suitable for repeated charge–discharge applications.[77] Moreover, the GCD profiles of both symmetric and asymmetric SCs at different current densities (1 to 15 A g^{-1}) in Fig. 15(c) and (d) match with the characteristic pseudocapacitive behavior.[55,78]

Furthermore, the performance of symmetric and asymmetric SCs was assessed in terms of specific capacitance (C_s), power density (P) and energy density (E), at a current density of 1 A g^{-1} using eqn (2)–(7) and the values are given in Table 1. In comparison, the symmetric SC demonstrates a doubled value of specific capacitance (83 F g^{-1}), while the asymmetric SC delivers the doubled values of both energy density (14.2 W h kg^{-1}) and power

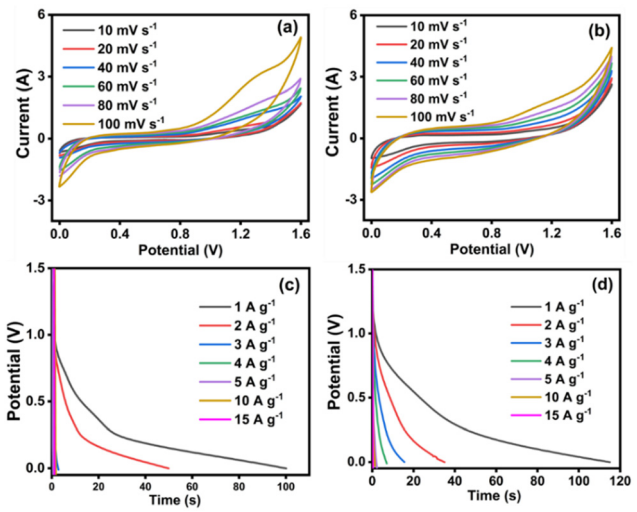

Fig. 15 The electrochemical performances of $NiMoO_4$/C (D50) based symmetric (left) and asymmetric (right) SCs: (a) and (b) CV curves at different scan rates, and (c) and (d) GCD curves at different current densities.

Table 1 Comparison of electrochemical performance of symmetric and asymmetric SCs at 1 A g^{-1}

Two-electrode SCs	C_s (F g^{-1})	E (W h kg^{-1})	P (W kg^{-1})
Symmetric	83	7.4	267
Asymmetric	40	14.2	444

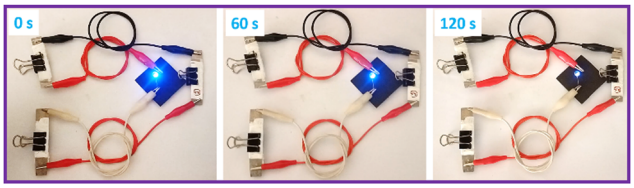

Fig. 16 Demonstration of powering a blue LED light by three $NiMoO_4$/C (D50) based symmetric SC devices connected in series.

density (444 W kg^{-1}). These outcomes highlight the promising electrochemical performance of $NiMoO_4$/C (D50) asymmetric SCs for versatile energy-storing applications.[44,57]

3.4. Fabrication of an all-solid-state symmetric SC

To demonstrate the practical energy storage capability of $NiMoO_4$/C (D50) in real-time, three symmetric supercapacitor devices were connected in series to power a blue LED (Fig. 16). This configuration successfully illuminated the LED for about two minutes, signifying their promising potential for practical applications where short-term bursts of energy are required. However, the observed decay of LED brightness is so fast due to the low-cost current collector (stainless-steel) used to fabricate all-solid-state symmetric supercapacitors. Furthermore, the electrolytes have to be optimized by a combination of different electrolytes for high-performing SCs.

Notably, the prepared $NiMoO_4$/C (D50) nanocomposite demonstrates a significant supercapacitor performance compared to previously reported $NiMoO_4$-based materials (Table S3, ESI†). This exceptional performance is due to several factors: (1) conductive carbon networks facilitate rapid charge/discharge, (2) the porous nanosphere structure maximizes electrolyte accessibility, boosting charge storage, (3) *in situ* synthesis and incorporation of optimal carbon content improves the electrolyte-philicity of the electrode *via* altering the surface composition and properties, providing more electroactive sites, and (4) intimate integration of $NiMoO_4$ and carbon amplifies supercapacitor behavior beyond individual component contributions. This rapid, one-pot, cost-effective, and environmentally friendly approach of *in situ* carbon incorporation enables scalable nanocomposite production, and promising applications in supercapacitors, lithium-ion batteries, and other energy storage technologies.

4. Conclusions

In summary, this work demonstrated the impact of different ratios of carbon in $NiMoO_4$/C (D*x*) nanocomposites prepared *via in situ* hydrothermal carbonization of dextrose for the application of electrode materials in supercapacitor

applications. The $NiMoO_4$/C (D50) nanocomposite exhibited a well-integrated structure, with $NiMoO_4$ nanorods dispersed within a graphitic carbon matrix, consisting of 71.1% $NiMoO_4$ and 28.9% carbon components. The graphitic carbon matrix showed increased defects with higher carbon content, which contributed to the enhanced surface area and mesoporosity of the nanocomposite. In particular, the $NiMoO_4$/C (D50) electrode material delivered a high specific capacitance of 940 F g^{-1} at 1 A g^{-1} compared to pure $NiMoO_4$ (520 F g^{-1}) and $NiMoO_4$/C (D10, D25 and D75) nanocomposites (436–583 F g^{-1}). Furthermore, the fabricated $NiMoO_4$/C (D50) based two-electrode system showed doubled energy and power densities (14.2 W h kg^{-1} and 444 W kg^{-1}) for asymmetric supercapacitors compared to symmetric supercapacitors (energy density of 7.4 W h kg^{-1} at power density of 267 W kg^{-1}). This noted superior supercapacitor performance of $NiMoO_4$/C (D50) can be ascribed to the incorporation of optimal carbon content in the nanocomposite, which synergistically improves the electroactive sites and electrolyte-philicity *via* altering the surface composition and properties of the electrodes, for more charge storage. Thus, this kind of *in situ* hydrothermal synthesis of bimetallic oxides/carbon nanocomposites with optimal carbon content using different carbon sources will be a promising strategy for achieving high-performance supercapacitors.

Data availability

The data supporting this article have been included as part of the ESI.†

Conflicts of interest

There are no conflicts to declare.

Acknowledgements

Dr S. Nehru gratefully acknowledges the financial support provided by the University of Madras (RUSA 2.0, RI & QI) and the DST-Science and Engineering Research Board (EEQ/2018/001402). Dr S. Veeralakshmi thanks the Department of Science and Technology, Ministry of Science and Technology, India, for the Women Scientist Scheme-A project (DST/WOS-A/CS-168/2021 (G)). Furthermore, the authors are thankful to the UGC DAE Consortium for Scientific Research, University Grants Commission, for the Collaborative Research Scheme (CRS) project (CRS/2021-22/04/629). We also express our sincere gratitude to the GNR Instrumentation Centre, University of Madras, for their invaluable analytical support.

Notes and references

1 R. A. Mir, S. Upadhyay, R. A. Rather, S. J. Thorpe and O. P. Pandey, *Energy Adv.*, 2022, **1**, 438–448.
2 S. Wang, W. Jiang, J. Wu, H. Huang, P. Guo, X. Zhang, H. Gu, Q.-A. Huang and Y. Hu, *Energy Adv.*, 2022, **1**, 704–714.
3 D. P. Chatterjee and A. K. Nandi, *J. Mater. Chem. A*, 2021, **9**, 15880–15918.
4 R. Patil, L. Pradhan, B. M. Matsagar, O. Agrawal, K. C. W. Wu, B. K. Jena and S. Dutta, *Energy Adv.*, 2023, **2**, 1650–1659.
5 B. Wang, Y. Wang, J. Park, H. Ahn and G. Wang, *J. Alloys Compd.*, 2011, **509**, 7778–7783.
6 J. Xu, J. Li, Q. Yang, Y. Xiong and C. Chen, *Electrochim. Acta*, 2017, **251**, 672–680.
7 K. Sasikumar and H. Ju, *Chemosensors*, 2022, **10**, 516.
8 Y. Huang, F. Cui, Y. Zhao, J. Lian, J. Bao, T. Liu and H. Li, *Inorg. Chem. Front.*, 2018, **5**, 1594–1601.
9 D. Cai, D. Wang, B. Liu, Y. Wang, Y. Liu, L. Wang, H. Li, H. Huang, Q. Li and T. Wang, *ACS Appl. Mater. Interfaces*, 2013, **5**, 12905–12910.
10 Y. Li, J. Jian, L. Xiao, H. Wang, L. Yu, G. Cheng, J. Zhou and M. Sun, *Mater. Lett.*, 2016, **184**, 21–24.
11 D. Guo, Y. Luo, X. Yu, Q. Li and T. Wang, *Nano Energy*, 2014, **8**, 174–182.
12 E. Murugan, S. Govindaraju and S. Santhoshkumar, *Electrochim. Acta*, 2021, **392**, 138973.
13 D. Cai, B. Liu, D. Wang, Y. Liu, L. Wang, H. Li, Y. Wang, C. Wang, Q. Li and T. Wang, *Electrochim. Acta*, 2014, **125**, 294–301.
14 C. Teng, X. Gao, N. Zhang, Y. Jia, X. Li, Z. Shi, Z. Wu, M. Zhi and Z. Hong, *RSC Adv.*, 2018, **8**, 32979–32984.
15 Y. Zhang, C.-R. Chang, X.-D. Jia, Q.-Y. Huo, H.-L. Gao, J. Yan, A.-Q. Zhang, Y. Ru, H.-X. Mei, K.-Z. Gao and L.-Z. Wang, *Inorg. Chem. Commun.*, 2020, **111**, 107631.
16 D. Muthu, S. Vargheese, Y. Haldorai and R. T. Rajendra Kumar, *Mater. Sci. Semicond. Process.*, 2021, **135**, 106078.
17 S.-W. Zhang, B.-S. Yin, C. Liu, Z.-B. Wang and D.-M. Gu, *Appl. Surf. Sci.*, 2018, **458**, 478–488.
18 M. Wang, J. Zhang, X. Yi, B. Liu, X. Zhao and X. Liu, *Beilstein J. Nanotechnol.*, 2020, **11**, 240–251.
19 E. R. Ezeigwe, P. S. Khiew, C. W. Siong, I. Kong and M. T. T. Tan, *Ceram. Int.*, 2017, **43**, 13772–13780.
20 M. Beemarao, P. Kanagambal, K. Ravichandran, P. Rajeswaran, I. M. Ashraf, U. Chalapathi and S.-H. Park, *Inorg. Chem. Commun.*, 2023, **153**, 110853.
21 C. Wei, Y. Huang, J. Yan, X. Chen and X. Zhang, *Ceram. Int.*, 2016, **42**, 15694–15700.
22 S. Zallouz, J.-M. Le Meins and C. Matei Ghimbeu, *Energy Adv.*, 2022, **1**, 1051–1064.
23 Z. Yang, J. Tian, Z. Yin, C. Cui, W. Qian and F. Wei, *Carbon*, 2019, **141**, 467–480.
24 S. A. Nicolae, H. Au, P. Modugno, H. Luo, A. E. Szego, M. Qiao, L. Li, W. Yin, H. J. Heeres, N. Berge and M.-M. Titirici, *Green Chem.*, 2020, **22**, 4747–4800.
25 Y. Mo, Q. Ru, X. Song, L. Guo, J. Chen, X. Hou and S. Hu, *Carbon*, 2016, **109**, 616–623.
26 L. Zhang, J. Mu, Z. Wang, G. Li, Y. Zhang and Y. He, *J. Alloys Compd.*, 2016, **671**, 60–65.
27 C. Wang, C. Wu, S. Chen, Q. He, D. Liu, X. Zheng, Y. A. Haleem and L. Song, *RSC Adv.*, 2017, **7**, 4667–4670.
28 H.-Y. Li, K. Jiao, L. Wang, C. Wei, X. Li and B. Xie, *J. Mater. Chem. A*, 2014, **2**, 18806–18815.

29 L. Ma, G. Sun, J. Ran, S. Lv, X. Shen and H. Tong, *ACS Appl. Mater. Interfaces*, 2018, **10**, 22278–22290.
30 Z.-H. Miao, H. Wang, H. Yang, Z. Li, L. Zhen and C.-Y. Xu, *ACS Appl. Mater. Interfaces*, 2016, **8**, 15904–15910.
31 Y. Qu, Z. Zhang, X. Wang, Y. Lai, Y. Liu and J. Li, *J. Mater. Chem. A*, 2013, **1**, 14306–14310.
32 R. Yuvaraja, S. Sarathkumar, V. Gowsalya, S. P. Anitha Juliet, S. Veeralakshmi, S. Kalaiselvam, S. Hussain and S. Nehru, *New J. Chem.*, 2024, **48**, 15556–15566.
33 Y. Zhou, C. Li, X. Li, P. Huo and H. Wang, *Dalton Trans.*, 2021, **50**, 1097–1105.
34 M. Sethi, U. S. Shenoy and D. K. Bhat, *Nanoscale Adv.*, 2020, **2**, 4229–4241.
35 Y. Qiu, X. Li, M. Bai, H. Wang, D. Xue, W. Wang and J. Cheng, *New J. Chem.*, 2017, **41**, 2124–2130.
36 M. Liu, Y. Yan, L. Zhang, X. Wang and C. Wang, *J. Mater. Chem.*, 2012, **22**, 11458–11461.
37 N. Padmanathan, H. Shao and K. M. Razeeb, *Int. J. Hydrogen Energy*, 2020, **45**, 30911–30923.
38 S. Ratha, A. K. Samantara, K. K. Singha, A. S. Gangan, B. Chakraborty, B. K. Jena and C. S. Rout, *ACS Appl. Mater. Interfaces*, 2017, **9**, 9640–9653.
39 V. S. Budhiraju, R. Kumar, A. Sharma and S. Sivakumar, *Electrochim. Acta*, 2017, **238**, 337–348.
40 E. Sulistya, L. Hui-Hui, N. K. Attenborough, S. Pourshahrestani, N. A. Kadri, E. Zeimaran, N. A. B. A. Razak, B. Amini Horri and B. Salamatinia, *J. Taibah Univ. Sci.*, 2020, **14**, 1042–1050.
41 J. Li, Y. Yang, Y. Xiao, B. Tang, Y. Ji and S. Liu, *Front. Mater.*, 2021, **8**, 790911.
42 N. Papaioannou, A. Marinovic, N. Yoshizawa, A. E. Goode, M. Fay, A. Khlobystov, M.-M. Titirici and A. Sapelkin, *Sci. Rep.*, 2018, **8**, 6559.
43 X. Xu, Q. Liu, T. Wei, Y. Zhao and X. Zhang, *J. Mater. Sci.: Mater. Electron.*, 2019, **30**, 5109–5119.
44 J. Yuan, D. Yao, L. Jiang, Y. Tao, J. Che, G. He and H. Chen, *ACS Appl. Energy Mater.*, 2020, **3**, 1794–1803.
45 S. Keerthana, B. J. Rani, R. Yuvakkumar, G. Ravi, B. Saravanakumar, M. Pannipara, A. G. Al-Sehemi and D. Velauthapillai, *Environ. Res.*, 2021, **197**, 111073.
46 G. Solomon, A. Landström, R. Mazzaro, M. Jugovac, P. Moras, E. Cattaruzza, V. Morandi, I. Concina and A. Vomiero, *Adv. Energy Mater.*, 2021, **11**, 2101324.
47 K. Thiagarajan, T. Bavani, P. Arunachalam, S. J. Lee, J. Theerthagiri, J. Madhavan, B. G. Pollet and M. Y. Choi, *Nanomaterials*, 2020, **10**, 392.
48 C. Hou, W. Yang, H. Kimura, X. Xie, X. Zhang, X. Sun, Z. Yu, X. Yang, Y. Zhang, B. Wang, B. B. Xu, D. Sridhar, H. Algadi, Z. Guo and W. Du, *J. Mater. Sci. Technol.*, 2023, **142**, 185–195.
49 Q. Mu, R. Liu, H. Kimura, J. Li, H. Jiang, X. Zhang, Z. Yu, X. Sun, H. Algadi, Z. Guo, W. Du and C. Hou, *Adv. Compos. Hybrid Mater.*, 2022, **6**, 23.
50 F. Li, Z. Bi, H. Kimura, H. Li, L. Liu, X. Xie, X. Zhang, J. Wang, X. Sun, Z. Ma, W. Du and C. Hou, *Adv. Compos. Hybrid Mater.*, 2023, **6**, 133.
51 Z. Zhang, Y. Liu, Z. Huang, L. Ren, X. Qi, X. Wei and J. Zhong, *Phys. Chem. Chem. Phys.*, 2015, **17**, 20795–20804.
52 M. Yao, Z. Hu, Y. Liu and P. Liu, *Ionics*, 2016, **22**, 701–709.
53 P. R. Jothi, S. Kannan and G. Velayutham, *J. Power Sources*, 2015, **277**, 350–359.
54 A. K. Yedluri, T. Anitha and H.-J. Kim, *Energies*, 2019, **12**, 1143.
55 C. J. Raj, R. Manikandan, K. H. Yu, G. Nagaraju, M.-S. Park, D.-W. Kim, S. Y. Park and B. C. Kim, *Inorg. Chem. Front.*, 2020, **7**, 369–384.
56 J. Wang, Y. Liu, T. Hao, J. Hao and T. Ma, *New J. Chem.*, 2024, **48**, 9778–9793.
57 Y. Hao, H. Huang, Q. Wang, Q. Wang and G. Zhou, *Chem. Phys. Lett.*, 2019, **728**, 215–223.
58 T. Liu, H. Chai, D. Jia, Y. Su, T. Wang and W. Zhou, *Electrochim. Acta*, 2015, **180**, 998–1006.
59 S. H. Kazemi, F. Bahmani, H. Kazemi and M. A. Kiani, *RSC Adv.*, 2016, **6**, 111170–111181.
60 L. Zhao and F. Ran, *Chem. Commun.*, 2023, **59**, 6969–6986.
61 M. Enterría, F. J. Martín-Jimeno, F. Suárez-García, J. I. Paredes, M. F. R. Pereira, J. I. Martins, A. Martínez-Alonso, J. M. D. Tascón and J. L. Figueiredo, *Carbon*, 2016, **105**, 474–483.
62 K. K. Lee, W. Hao, M. Gustafsson, C.-W. Tai, D. Morin, E. Björkman, M. Lilliestråle, F. Björefors, A. M. Andersson and N. Hedin, *RSC Adv.*, 2016, **6**, 110629–110641.
63 L. Su, J. Li and F. Ran, *Green Chem.*, 2023, **25**, 9351–9362.
64 S. Veeralakshmi, S. Kalaiselvam, R. Murugan, P. Pandurangan, S. Nehru, S. Sakthinathan and T.-W. Chiu, *J. Mater. Sci.: Mater. Electron.*, 2020, **31**, 22417–22426.
65 T. Dong, M. Li, P. Wang and P. Yang, *Int. J. Hydrogen Energy*, 2018, **43**, 14569–14577.
66 B. Tong, W. Wei, X. Chen, J. Wang, W. Ye, S. Cui, W. Chen and L. Mi, *CrystEngComm*, 2019, **21**, 5492–5499.
67 F. Ran, Y. Wu, M. Jiang, Y. Tan, Y. Liu, L. Kong, L. Kang and S. Chen, *Dalton Trans.*, 2018, **47**, 4128–4138.
68 V. Sharma, R. V. Khose and K. Singh, *Energy Adv.*, 2024, **3**, 177–190.
69 R. Deka, S. Rathi and S. M. Mobin, *Energy Adv.*, 2023, **2**, 2119–2128.
70 M. Salihovic, E. Pameté, S. Arnold, I. Sulejmani, T. Bartschmid, N. Hüsing, G. Fritz-Popovski, C. Dun, J. J. Urban, V. Presser and M. S. Elsaesser, *Energy Adv.*, 2024, **3**, 482–494.
71 P. N. K. Siddu, S. M. Jeong and C. S. Rout, *Energy Adv.*, 2024, **3**, 341–365.
72 A. Pullanchiyodan, R. Joy, P. Sreeram, L. R. Raphael, A. Das, N. T. M. Balakrishnan, J.-H. Ahn, A. Vlad, S. Sreejith and P. Raghavan, *Energy Adv.*, 2023, **2**, 922–947.
73 Z. Guo, Y. Zhao, J. Mu, S. Li, F. Li, J. Wang, H. Yang, J. Mu and M. Zhang, *Ceram. Int.*, 2023, **49**, 19652–19663.
74 Z. Luo, D. Shu, F. Yi, J. Ling, M. Wang, C. Huang and A. Gao, *New J. Chem.*, 2021, **45**, 22748–22757.
75 R. Liu, X.-R. Shi, Y. Wen, X. Shao, C. Su, J. Hu and S. Xu, *J. Energy Chem.*, 2022, **74**, 149–158.
76 P. Kumcham, T. V. M. Sreekanth, K. Yoo and J. Kim, *New J. Chem.*, 2024, **48**, 7820–7835.
77 D. Jhankal, M. S. Khan, P. Shakya, N. Bhardwaj, B. Yadav, K. K. Jhankal and K. Sachdev, *Energy Adv.*, 2024, **3**, 191–202.
78 Z. Wang, G. Wei, K. Du, X. Zhao, M. Liu, S. Wang, Y. Zhou, C. An and J. Zhang, *ACS Sustainable Chem. Eng.*, 2017, **5**, 5964–5971.